Comparative Study of Short Term Diurnal Tidal Variability

H.-L. Liu,[1,2] T. Li,[3,4] C.-Y. She,[3] J. Oberheide,[5] Q. Wu,[1,2] M. E. Hagan,[1] J. Xu,[2] R. G. Roble,[1] M. G. Mlynczak,[6] and J. M. Russell III,[7]

H.-L. Liu, High Altitude Observatory, National Center for Atmospheric Research, P.O.Box 3000, Boulder, CO 80307-3000, USA. (liuh@ucar.edu)

[1]High Altitude Observatory, National

Abstract. The wind and temperature measurements from an unusually long period operation of the sodium lidar at Colorado State University (41°N, 105°W) around September equinox 2003 showed significant short term tidal variability. Coincident with the large tidal changes, a strong temperature inversion layer was also observed above 90 km. Examination of the simulta-

Center for Atmospheric Research, Boulder, Colorado, USA.

[2]State Key Laboratory for Space Weather, Chinese Academy of Sciences, Beijing, China

[3]Physics Department, Colorado State University, Fort Collins, Colorado, USA.

[4]Currently at NASA-JPL, California Institute of Technology, Wrightwood, California, USA.

[5]Physics Department, Wuppertal University, Wuppertal, Germany.

[6]NASA Langley Research Center, Hampton, Virginia, USA

[7]Hampton University, Hampton, Virginia, USA

neous temperature measurement from the Sounding of the Atmosphere using Broadband Emission Radiometry (SABER) instrument, on board of the Thermosphere Ionosphere Mesosphere Energetics and Dynamics (TIMED) satellite, not only confirms the existence of the inversion layer but also reveals the global nature of the inversion, suggesting the presence of a transient planetary wave in the mesosphere. The large tidal variability, therefore, is probably a consequence of the interaction between the transient planetary wave and tides. This possibility is investigated by using the NCAR thermosphere-ionosphere-mesosphere-electrodynamics general circulation model (TIME-GCM) and by comparing model results with the lidar, SABER, and TIMED Doppler Interferometer (TIDI) measurements. With a large transient planetary wave specified at the model lower boundary, the model is able to produce strong diurnal tidal variability comparable to that from the lidar observation, and the modeled temperature inversion is similar to that from the SABER measurement. The model results suggest that the planetary/tidal wave interaction excites non-migrating tides and modulates the gravity modes and/or the rotational modes of the diurnal migrating tide. Among the non-migrating tides, the diurnal zonally symmetric (S=0) component is the strongest, and its interaction with the planetary wave leads to a strong diurnal eastward wavenumber 1 component.

1. Introduction

Atmospheric tides are important sources of variability in the mesosphere, thermosphere, and ionosphere. The tidal amplitudes, and to a lesser degree their phases, also display significant variability on time scales ranging from day-to-day to inter-annual. Regarding the short-term variability, which is the focus of the current study, frequency analyses of ground-based observations from single or multiple sites have shown the modulation of tides on time scales of planetary waves (from quasi-two-day to quasi stationary) [*Nakamura et al.*, 1997; *Kamalabadi et al.*, 1997; *Jacobi*, 1999; *Pancheva*, 2000; *Pancheva and Mukhtarov*, 2000; *Pancheva et al.*, 2000, 2002; *Pancheva and Mitchell*, 2004; *She et al.*, 2004; *Pancheva*, 2006; *Nozawa et al.*, 2006]. Related spectral analyses also suggest nonlinear interactions between the tides and planetary waves. Specifically, the nonlinear interaction between tides and quasi-stationary planetary waves has been proposed as an important mechanism for exciting non-migrating tides and causing large short term tidal variability [*Hagan and Roble*, 2001; *Oberheide et al.*, 2002; *Liu and Roble*, 2002; *Mayr et al.*, 2003; *Ward et al.*, 2005; *Mayr et al.*, 2005a, b]. This mechanism is supported by the tidal and planetary wave analyses of temperature from Nimbus-7 Limb Infrared Monitor of the Stratosphere (LIMS) and CRyogenic Infrared Spectrometers and Telescopes for the Atmosphere (CRISTA) [*Oberheide et al.*, 2002; *Lieberman et al.*, 2004], and winds from the High Resolution Doppler Imager (HRDI) and TIDI [*Angelats i Coll and Forbes*, 2002; *Oberheide et al.*, 2006b]. Another important source of non-migrating tides, thus a source of tidal variability, is tropospheric latent heat release [*Hagan et al.*, 1997; *Forbes et al.*, 1999; *Oberheide et al.*, 2002; *Hagan and Forbes*, 2002, 2003; *Ward et al.*, 2005]. The relative role of planetary/tidal wave interaction and latent heat release in non-migrating tidal excitation has also been studied [*Oberheide et al.*, 2002]. By analyzing the observations from the SABER and TIDI instruments on board the TIMED satellite, *Zhang et al.* [2006] and *Oberheide et al.* [2006b] showed that the non-migrating components in the mesosphere and lower thermosphere (MLT) could reach amplitudes comparable to the migrating components. Recent studies also suggest that interaction between the gravity waves and tides could also cause large tidal variability, both locally and globally [*Liu and Hagan*, 1998; *Liu et al.*, 2000; *Mayr et al.*, 2003; *Ortland and Alexander*, 2006].

Because of their high temporal resolution and extended vertical coverage, ground-based measurements are often used to study the short-term tidal variability and coupling between tides and planetary waves. As mentioned above, the short-term tidal variability could result from tidal interactions with either planetary waves or gravity waves and could be either global or local. It is thus necessary to obtain spatial information in the horizontal direction to unambiguously determine the nature of the interaction. This, however, cannot be done with ground-based observation at a single site. To overcome the lack of spatial information in the horizontal direction, networks of ground-based measurements have been used [e.g. *Nakamura et al.*, 1997; *Pancheva et al.*, 2000, 2002; *Murphy et al.*, 2003]. Ground-based measurements involving imagery measurements are also often limited to night coverage. This makes it difficult to study the diurnal tide and its short-term variability, though recent advancement in lidar technology has enabled continuous 24-hour measurements (weather permitting) [*Chen et al.*, 1996]. Satellite observations, on the other hand, have global or nearly global spatial coverages, but are often limited in their local time coverage because of their near sun-synchronous orbits. It often takes more than 30 days for the satellites to complete one full 24-hour local time coverage, and information of short-term tidal variability is hard to extract from these measurements. A recently developed non-Fourier method [*Oberheide et al.*, 2002] allows tidal analysis of satellite data on a daily basis, but the method critically depends on data quality and orbit geometry such that it can only be applied in certain cases. It is thus evident that the ground-based and satellite observations are complementary in their measurement capabilities, and it is desirable to compare and synthesize the two sets of observations in studying tides and their short-term variability [*Azeem et al.*, 2000].

In this study, we examine tidal variability around the September equinox of 2003 by comparing a period of unusually long lidar observation with simultaneous satellite observations and targeted numerical simulations. *She et al.* [2004] reported that the Colorado State University (CSU) sodium lidar obtained a data set between Sep 18 and Oct 1 2003 (DOY 261-274), including a 9-day continuous observation. Their analyses of this unique data set revealed very large short-term tidal variability. Between DOY 266 and 268, the diurnal and semi-diurnal tidal amplitudes increase by factors of 2-3, and a strong temperature inversion was observed around 90 km during the same time period. Apart from tidal periods, they also identify oscillations with periods of 1.5, 3, and 5 days, as well as 10, 14, and 20 hours. These were interpreted as signatures of planetary waves (PW) and/or PW interaction with tides. From ground observations at a single site, however, it is difficult to determine unambiguously whether the tidal variability results from PWs/tides interaction [e.g *Hagan and Roble*, 2001] or local interactions between mesoscale gravity waves (GWs) and tides [e.g. *Liu and Hagan*, 1998]. In this study, we examine the presence of PWs for this period of time using the temperature and wind observations from the SABER and

TIDI instruments, and the cause of the tidal variability using the NCAR Thermosphere, Ionosphere, Mesosphere, Electrodynamics General Circulation Model (TIME-GCM) simulations. From the TIME-GCM simulations, we study the changes of various modes associated with the migrating diurnal tide as well as the non-migrating components.

In section 2, brief descriptions of the CSU lidar system, TIMED/SABER and TIDI instruments, and the NCAR TIME-GCM will be given. The observational evidence of large short-term tidal variability and presence of planetary wave(s) will be presented in section 3. Results from the targeted numerical experiments using TIME-GCM will be analyzed and compared to the observations in section 4. Section 5 is the conclusion.

2. Description of Instruments and Numerical Model

2.1. CSU Sodium Lidar System

The current Colorado State University sodium lidar system is a three-frequency, two-beam system enabling 24-hour continuous, simultaneous observations of the mesopause region temperature, zonal wind, and meridional wind as well as sodium density. The system receiver employs two 14-inch Celestron telescopes pointing eastward and northward, both at 30° from zenith. The lidar transmitter directs two laser beams into the atmosphere, each aligned parallel to one telescope. In comparison to other lidar systems, the CSU sodium lidar system has a modest power-aperture product of 0.05 Wm^2. However, due to the resonance enhancement in laser induced fluorescence, the received signal is sufficient to probe atmospheric instabilities, as well as various atmospheric waves and their interactions [*She et al.*, 2004; *Li et al.*, 2005]. The precision of the measurements for temperature and wind with 2-km vertical resolution and 1-hour temporal resolution is estimated to be 0.5 K and 1.5 ms^{-1}, respectively, at 92 km (sodium peak), and 5 K and 15 m^{-1}, respectively, at both 81 km and1 05 km (sodium layer edges), under nighttime clear sky conditions. For the daytime measurement, the Faraday filter is used in the receiver channels to efficiently reduce background by a factor of 6000-8000, which also reduces signal by a factor of 4-5 [*Chen et al.*, 1996]. Therefore, the uncertainty of the daytime measurements increases by at least a factor of 2.5 in comparison to the nighttime measurements.

For the study of tidal variability in *She et al.* [2004] and in this study, a 9-day continuous observation around 2003 September equinox (days 264-273) with 2km vertical resolution and 15min and 30min temporal resolutions respectively for nighttime and daytime was analyzed by performing tidal analysis over the individual 24-hour dataset centered at each hour.

2.2. TIMED/SABER Instrument

As one of four key instruments onboard TIMED, SABER remotely sounds the temperature distribution from the lower stratosphere to the lower thermosphere, daily and near globally. It also measures O_3, H_2O and CO_2 mixing ratio vertical profiles and key energetics parameters describing upper atmosphere heating, cooling and airglow losses [*Russell et al.*, 1999]. Temperature is measured using three channels in the 15 μm and 4.3 μm CO_2 bands while the remaining seven SABER channels cover the range from 1.27 μm to 9.6 μm. Non-local thermal equilibrium (non-LTE) of CO_2 emissions above 75 km has been accounted for in the temperature retrieval [*Mertens et al.*, 2001, 2004]. The data measured by SABER, including temperatures in the MLT, have been available since early 2002. The version of the data used in this analysis is v01.06.

2.3. TIMED/TIDI Instrument

As another key instrument of the four on the TIMED satellite, TIDI provides basic information about global vector winds in the mesosphere and lower thermosphere (MLT). The TIDI instrument was developed and built at the University of Michigan [*Killeen et al.*, 1999]. TIDI measures neutral winds by performing limb scans of various upper atmosphere airglow layers and monitoring the Doppler shift of airglow emissions induced by neutral winds. TIDI is an instrument with four telescopes, a circle to line interferometer (CLIO) conical mirror, and a CCD detector with quantum efficiency exceeding 60% at some wavelengths. The four TIDI telescopes are orthogonally oriented, allowing the instrument to measure neutral wind vectors on both sides of the satellite track. More information about TIDI measurements can be found in *Wu et al.* [2006] and *Killeen et al.* [2006]. The neutral wind data used for this paper are obtained by using the preliminary O_2 P9 filter data processed at NCAR/HAO. The daytime data cover the 70-115 km altitude range. The horizontal resolution of the data in the meridional direction is roughly 7 degrees and the vertical resolution is 2.5 km. The TIMED satellite orbits the Earth 15 times per day and each side (cold, facing away from the sun; warm, facing towards the sun) samples 15 different longitude locations at approximately the same local time in lower and mid-latitudes. We used the data from the coldside ascending orbit node for this study, which was in the daytime. The data from 15 orbits during a day are used to examine the longitudinal variations.

2.4. NCAR TIME-GCM and Satellite and Model Sample Extraction

NCAR TIME-GCM is a three-dimensional time-dependent model that simulates the circulation, temperature, and compositional structure from the upper stratosphere to the thermosphere. It combines all the previous features of the TGCM [*Dickinson et al.*, 1981, 1984], TIGCM [*Roble et al.*, 1988], and TIE-GCM [*Richmond et al.*, 1992], and includes aeronomical processes appropriate for the mesosphere and upper stratosphere [*Roble et al.*, 1987; *Roble and Ridley*, 1994; *Roble*, 1995]. For this study, a horizontal resolution of $5^\circ \times 5^\circ$ is used and there are 45 pressure surfaces extending from 10 hPa ($\sim$30 km height) to $\sim$500 km with a vertical resolution of 2 grid points per scale height. Details of the numerical framework of the model can be found in *Dickinson et al.* [1981]. Diurnal and semi-diurnal tidal components due to tropospheric forcing are specified at the lower boundary with the Global Scale Wave Model (GSWM) [*Hagan et al.*, 1999]. The gravity wave effects in TIME-GCM need to be parameterized and the parameterization is based on linear saturation theory by *Lindzen* [1981]. For this study, the lower boundary conditions are specified without and with planetary wave perturbation, referred to as base case and control case, respectively, as will be discussed in section 4.

To facilitate direct comparison between model results and satellite observations, diagnostic tools have been developed to perform Satellite and Universal Time (SATUT) sampling of the TIME-GCM results. The basic idea of the SATUT sampling is to provide winds, temperatures, and trace constituents that would be measured if the satellite flew through the model atmosphere. Model fields not directly observed by the satellite can also be provided. Locations (latitude and longitude) and Universal Time (UT) of the instrument footprints are extracted from the observed data. The TIME-GCM hourly model histories are then linearly interpolated in space and time to the instrument footprints. Model results associated with missing or “bad” observational data are treated as missing values and are not sampled. TIME-GCM has been sampled along the footprints of several satellite instruments, including the SABER and TIDI. Selected data sets sampled for SABER and TIDI may be downloaded from http://timed.hao.ucar.edu/cedar/satut/. Applications include estimates of tidal aliasing in SABER temperatures [*Oberheide et al.*, 2003] and the analysis of non-migrating tides in TIDI winds [*Oberheide et al.*, 2006b].

3. Observations

As the tidal analysis in *She et al.* [2004] indicates, the amplitudes of the mesospheric diurnal and semi-diurnal tides above the observation site went through tremendous variability within the 9-day period, especially between days 267-269. The amplitude and phase (i.e., the local time when the signal peaks) of the diurnal temperature and zonal wind oscillations obtained from CSU lidar observations are shown in Figure 1. At 90 km, the amplitude of the diurnal temperature signal increases from about 6 K on day 266 to 18 K on day 267 and then drops to 2 K on day 269. The phase varies by about 4 to 5 hours between day 266 and 269. The amplitude of the diurnal zonal wind oscillates between 10 and 30 ms^{-1} between day 264 and 267, and then increases from 10 ms^{-1} on 267 to 43 ms^{-1} on 268. Its phase, lagging that of the temperature by about 5 hours, varies by about 5-6 hours.

Coincident with the large tidal variability, the lidar observation also shows the presence of a strong mesospheric inversion layer (MIL) between 85-90 km on days 267 and 268 (Figure 5a in *She et al.* [2004]). The large tidal variability could result from the local changes of apparent tidal amplitude and phase from tidal-gravity wave interactions, or excitation of non-migrating tides from tidal-planetary wave(s) interactions [e.g. *Liu and Hagan*, 1998; *Hagan and Roble*, 2001]. Similarly, MILs could form on both mesoscales and planetary scales [e.g *Liu and Hagan*, 1998; *Liu et al.*, 2000; *Salby et al.*, 2002; *Sassi* *et al.*, 2002; *Oberheide et al.*, 2006a]. From a ground-based perspective at a single site, however, it is difficult to distinguish between the two possibilities [*Liu and Meriwether*, 2004]. This uncertainty prompts us to examine the global observations from the SABER and TIDI instruments during the same time period.

Figure 2 shows the temperature measured by SABER at 40°N on days 266, 267 and 268. Note that the data from the ascending orbit node corresponds to 11 hours local time (LT) and the descending orbit node to LT23 hour. As demonstrated in previous study by *Xu et al.* [2006], the SABER temperature at 105°W is statistically in agreement with the lidar measurements. On day 267 and at LT23, a MIL can be seen above the lidar site in SABER temperature with the maximum temperature of ~205 K at 88 km and minimum temperature of ~160 K at 100 km. This is similar to the temperature profiles obtained from the CSU lidar measurements (Figure 5 in *She et al.* [2004]). It is evident from Figure 2 that the MIL has a large-scale structure in the longitudinal direction, and it varies quite rapidly with day as well as local time. The strongest warm anomaly of 225 K is observed at 90°E and 86 km in the descending node on day 267. A weaker warm anomaly occurs between 100°W to 150°W at similar altitudes, which is seen in the lidar measurement. The lapse rates above the two warm anomalies, however, are similar, because the atmosphere is generally colder in the western hemisphere at higher altitudes. On the following day, the warm anomaly and the MIL are not as strong but still stronger than those on day 266 (note the color scales are different for the three days). For all three days, the peak temperatures of the MIL are located between 80-90 km.

The longitudinal phases of the temperature perturbations at the ascending and descending orbit nodes are similar, but the magnitudes are different. This local time dependence suggests the tidal modulation of temperature structures. Further, the longitudinal variations of the temperature and MIL in both ascending and descending orbit nodes imply the presence of planetary wave(s) and/or non-migrating tidal components, because TIMED satellite is almost sun-synchronous. Longitudinal variations are also clearly seen in the meridional and zonal winds from TIDI observations (Figure 3) on days 264, 267 and 268 (data gaps are large on days 265 and 266). The meridional wind between 100-120 km in the western hemisphere from TIDI is consistently large ($\geq$100 ms^{-1}) on days 264, 267 and 268. It is not clear if this indeed reflects an extremely strong wavenumber 1 feature in this altitude range, though it is qualitatively consistent with the large longitudinal temperature gradient seen in Figure 2 in the same region. The longitudinal structures also indicate westward tilting in both temperature (between 10-100°E in the descending orbit node) and wind fields (western hemisphere) on day 267. This is another indication of the presence of planetary waves. According to *Salby et al.* [2002] and *Sassi et al.* [2002], large temperature anomalies can occur in the mesosphere where the planetary wave varies rapidly with altitude. This is because the temperature perturbation is proportional to the vertical gradient of the geopotential height perturbation under the hydrostatic assumption. It should be noted that abrupt temperature changes are seen at 70°E and 130°W on day 266 and 267, respectively, at the descending orbit node. It is not clear what causes these abrupt changes, and we have confirmed the local time difference between profiles used to construct the longitude-height cross-section is small. Further, sampling of TIME-GCM results using the SABER orbit data (discussed later) does not yield such abrupt changes.

If the large scale temperature anomalies are manifestations of planetary wave perturbations, then the rapid change of the MIL magnitudes may indicate that the planetary wave is transient, peaking around day 267 in the mesosphere. Transient planetary waves have been demonstrated to cause large mesospheric variability around fall equinox [*Taylor et al.*, 2001; *Liu et al.*, 2001].

It is thus possible that both the MIL and the large short-term tidal variability around day 267 result from a transient planetary wave and its interaction with tides. We further examine this possibility by conducting TIME-GCM experiments.

4. Numerical Experiments Using TIME-GCM

Two sets of numerical experiments are performed using the NCAR TIME-GCM. The base case is a climatological simulation for the period of day 255-275, and the only planetary scale perturbations specified at the lower boundary of the model are migrating tides from GSWM. In the control case, a zonal wavenumber 1 wave with stationary phase and time varying amplitude is specified at the lower boundary in addition to the tides. The temporal evolution of the wave amplitude is Gaussian, peaking on day 261 with a half width of 2 days. Because the wave amplitude is time varying and Gaussian, the wave projects on a Gaussian spectrum in the frequency space. The wave amplitude maximizes at 60°N. The maximum geopotential height perturbation of the wave on day 261 at 60°N is 2000 m. It should be noted that these wave characteristics are not inferred from the observations mentioned above, and in this work we will conduct qualitative rather than quantitative comparisons between the observations and model simulations. The primary goal is to understand if and how a transient planetary wave can induce short-term tidal variability of observed qualitative characteristics.

We first sample the temperature and winds of the control case using the SATUT tool. Figure 4 shows the sampling of temperature on day 267 and of winds on day 268. The longitudinal structures (predominantly wavenumber 1), as well as their westward tilt, are qualitatively similar to those observed in Figures 2 and 3. Some detailed structures are also reproduced in the simulation. For example, a strong warm anomaly is seen at 90°E and a weaker one around 90°W at slightly higher altitude for the ascending orbit node, and the temperature is warmer in the eastern hemisphere at the mesopause (∼100 km). As with SABER observations, there are also differences between the temperature structures measured during the ascending and descending orbit nodes. The strong warm anomaly, however, is observed at the descending node by the satellite, while it appears in the ascending node in the sampled model results. This suggests that the phase of the diurnal tide at this altitude may not be correctly reproduced in the model. The magnitude of the strong warm anomaly and the strength of MIL are much weaker in the model results as compared with the observations, indicating that the amplitudes of the planetary wave or tides are underestimated and/or the vertical variation of geopotential height perturbation of the planetary wave is not as strong in the simulation. In addition to variations with longitudes, vertical variations are also seen in temperature and winds. A vertical wavelength between 20-25 km can be inferred from TIDI observations (Figure 3), which are likely signatures of the diurnal tide [e.g. *Forbes*, 1995]. The vertical wavelength from the sampled model winds (Figure 4) is larger.

The diurnal components of temperature and zonal wind perturbations are now examined. Figure 5 shows the total diurnal temperature and zonal wind amplitudes on day 267 derived from the base and control simulations. These results are obtained by applying

FFT to the 24 hours of model results for the latitude-height cross-section at 105°W. What is shown is the amplitude of the 24-hour component, and thus includes contributions from both diurnal migrating and non-migrating components. Because the amplitude is obtained at a single longitude, it is similar to the sampling that would be obtained by ground-based observations with 24-hour coverage. In the base case, the temperature amplitude has a primary peak at the equator, minimum values (nodes) near 20°, and secondary peaks around 30°. The peak of the zonal wind amplitude varies slightly between 20° and 30° with altitude (the zonal wind peak of the (1,1) mode is at 24° according to classical tidal theory [*Forbes*, 1995]). Both amplitudes grow with altitude to the maximum values at about 100-105 km. These latitude and height structures are similar to those of the migrating diurnal tide, which is thus the main contributor to the diurnal perturbations in the base case. These structures, however, change quite significantly with the presence of the planetary wave, with the amplitudes generally being enhanced and the location of the peak amplitudes being shifted.

The simulated time evolution of the diurnal temperature and zonal wind at ~91 km altitude near the CSU lidar site is shown in Figure 6. In the control case (solid line), the diurnal temperature amplitude goes through large and rapid changes between day 260 and 275. The amplitude increases from 7 K to about 14 K from day 265 to 266, falls back to 7 K on day 269, and then further drops to 5 K on day 271. For comparison, the diurnal temperature amplitude stays between 6-7 K in the base case (dotted line). The phase of the diurnal temperature signal in the control case deviates from the base by up to 4 hours. The increase of the diurnal zonal wind amplitude is also large after day 265, from 20 ms^{-1} to 36 ms^{-1} on day 268. This amplitude in the base case is around 20 ms^{-1}. The phase of the diurnal zonal wind lags that of the diurnal temperature by about 5 hours, and displays a similar range of variability in the control case.

By comparing Figures 1 and 6, it is recognized that the qualitative features of the observed large short-term tidal variability are reproduced in the control case. The most prominent features include the rapid and large increase/decrease of the diurnal amplitudes and the range of variation of the tidal phase. Another similarity between the observation and the simulation is the occurrence of the peak temperature amplitude prior to the peak zonal wind amplitude. The phase values of the diurnal temperature and zonal wind are different from the observations, as indicated in the comparisons with SABER and TIDI observation. This is probably caused by the inaccurate representation of the tidal vertical wavelength in the TIME-GCM. The relative phase difference between the diurnal temperature and zonal wind in the model, on the other hand, is similar to that found in the observation.

The diurnal perturbations from the two simulations are then decomposed into migrating and non-migrating components using a 2D FFT analysis in time and longitude. The migrating, eastward wavenumber 1 (E1), wavenumber 0 (i.e. zonally symmetric, S=0), and westward wavenumber 2 components of diurnal temperature perturbations (W2) at 91 km and 42.5°N are shown in Figure 7. It is noted that in the base case the non-migrating components are very small except at high latitudes above 100 km due to auroral forcing (not illustrated). As expected from the work by *Hagan and Roble* [2001], non-migrating components (S=0 and W2) are generated from the nonlinear interaction between the planetary wave with zonal wavenumber 1 and the migrating tide. The S=0 component is particularly strong (peak value larger than 10 K). This is probably why the E1 component, resulting from secondary nonlinear interaction between the S=0 component and the stationary planetary wave 1 (SPW1), also becomes large. In addition to the non-migrating components, the amplitude of the migrating component is also modulated by its interaction with the planetary wave (and probably with the non-migrating components too). At this specific height and latitude, the amplitude of the migrating component is larger than that in the base case on days 262-267 and 269.5-274, and lower on days 267-269.5. The magnitude of the variation is comparable to those of the non-migrating components. For example, another product of the abovementioned secondary nonlinear interaction between the S=0 component and the SPW1 is the migrating diurnal tide. This may explain why the large modulation of the migrating diurnal tide coincides with the peak of the E1 component on day 268 (Figure 7). The results also indicate that the growth or decaying rates of these migrating and non-migrating components differ and, as a result, the magnitude and time of their respective peaks vary. Even though both the diurnal S=0 and W2 components are excited by the interaction between migrating diurnal tide and SPW1, their amplitudes and the variation are different. This could be caused by the different latitudinal structure, different propagating condition, and different dissipation rate for each component. Further, each component could be involved in various additional nonlinear triad (e.g. diurnal S=0, SPW1, and E1). This may explain that the S=0 and W2 components do not track each other, especially when the E1 component is strong. The changes shown in Figure 7 are local manifestation of variations on global scales (Figure 8). It is also clear from Figure 8, which is obtained from 2D FFT in the time-longitude domain at each latitude and height, that the modulation of the migrating tidal amplitude has a clear spatial pattern, with the amplitude enhanced in certain regions and weakened in others.

The non-migrating tidal components are enhanced above 70 km at most latitudes, though the magnitude and latitudinal structures differ among these components.

The relationship between the propagation of the planetary wave and the change of various tidal components can be clearly seen in the geopotential height perturbations (Figure 9). The planetary wave (wave 1) propagates upward and its amplitude at 100 km grows to a maximum value of 1200 m on day 264, about 3 days after it peaks at ~30 km. Afterword, the planetary wave in the MLT region does not follow the wave source which gradually decays away, but rather reaches extremas of 600 m and 800 m on days 267 and 271, respectively. The growth of the non-migrating components with time follows the upward propagation of the planetary wave energy, though their growth rate and time reaching their respective maximums are different. For the migrating diurnal components, two latitudes (2.5°N and 52.5°N) are examined. At both latitudes, the amplitudes of the migrating diurnal tide display modulation patterns with a period of about 6-7 days, but the spatial scales of the patterns in the vertical direction are different. At the equator, the vertical distance between adjacent positive and negative peaks is about 13 km, approximately equal to the half wavelength of the (s=1,n=1) mode of migrating diurnal tide, s and n being the zonal wavenumber and order of the eigenfunction, respectively [e.g *Forbes*, 1995]. The vertical structure of the modulation is much deeper at 52.5°N. This dependence of the vertical structures on the latitudes implies that different modes of the migrating diurnal tide are affected by the interactions with the planetary wave.

According to the classical tidal theory [*Chapman and Lindzen*, 1970; *Forbes*, 1995], the latitudinal structure of tide can be decomposed into Hough functions, which are eigenfunctions of the Laplace tidal equation and form a complete set of orthogonal functions. To elucidate the interactions of its various modes with the planetary wave, the migrating diurnal tide is projected onto 8 Hough functions (modes): 4 gravity modes (1,1), (1,2), (1,3), and (1,4) and 4 rotational modes (1,-1), (1,-2), (1,-3), and (1,-4). Figure 10(a) shows the migrating diurnal tide in geopotential height from the base case simulation on day 267 (similar for other days), and (b), (c) and (d) are the projection on the (1,1), (1,-1) and (1,-2) modes. It is evident that the (1,1) mode is most prominent at lower latitudes, and the trapped modes becomes stronger at higher latitudes. Because these modes represent specific spatial information in the latitude direction, such as the latitudinal nodes and symmetry with respect to the equator, projection of the diurnal migrating tide onto these modes provides a way to quantify the change of the latitudinal structure of the tide and contribution to the migrating tidal variability from these modes at various latitudes. Figure 11 shows the partition of the migrating diurnal tidal perturbation of the geopotential height at 42.5°N and 100 km altitude in terms of these modes. At this mid-latitude location, the rotational modes, especially (1,-2) the first symmetric trapped diurnal tide, constitute the bulk of the short term variability of the migrating diurnal tide. On day 264, for example, the difference of the total geopotential height perturbation of the migrating diurnal component between the control and base cases is 140 m, and the differences due to (1,-2) and (1,-1) modes are near 100 m and $\sim$35 m, respectively. Figure 12 shows the differences in the perturbation amplitudes (i.e. the eigenvalues multiplied to the corresponding Hough modes) of the (1,1), (1,-1) and (1,-2) on day 264. The latitudinal structures of the amplitude modulation reflect those of the Hough modes, with the maximum amplitudes of the gravity modes located at the equator or low latitudes and those of the rotational modes at middle and high latitudes ((1,-1) and (1,-2) peak near 45° and 55° respectively according to classical tidal theory). With trapped modes as an indicator of forcing region of the tides, the large variability of the trapped modes is also consistent with the strong interaction between planetary wave and tide at high latitudes. The vertical scale of the amplitude modulation is probably dependent on the vertical scales of the tidal modes and of the planetary wave. Because the rotational modes are trapped modes, the vertical scales of the modulation patterns are much larger than those of the propagating modes. Figure 13 shows the modulation of these modal amplitudes over time at the latitudes where these modulations are strong. By comparing them to Figure 9, it is seen that they account for most of the total variations of migrating diurnal amplitudes and the difference in vertical scales at different latitudes.

The temporal changes in Figures 9, 11, and 13 all indicate that the modulation of the respective amplitudes has a period of 6-7 days (also confirmed by wavelet analysis), even though the specified phase of the planetary wave is stationary. This is probably due to preferential excitation by the transient planetary wave, which excites a continuous frequency spectrum. According to previous studies by *Talaat et al.* [2001] and *Liu et al.* [2004], the atmospheric condition around equinox is favorable for the westward wave with wavenumber 1 and period between 5-7 days to propagate from the lower atmosphere to the MLT and to amplify therein. This is also supported by the latitudinal structure of the amplitude of the wavenumber 1 zonal wind component in the later stage of the simulation (after day 268), which has a major peak at the equator and secondary peaks at 50°, resembling the latitudinal structure of the first symmetric mode of the Rossby wave [*Talaat et al.*, 2001]. This wave is probably also responsible for the 6-7 day period in the tidal amplitude variation, though the detailed mechanism is not clear. Oscillations with various periods are also identified from the CSU lidar observation in the 9-day continuous observation period [*She et al.*, 2004], but it is difficult to unambiguously determine periods of 6-7 days or longer.

From Figures 8, 9, 12, and 13, the most prominent variability due to the planetary wave and its interaction with the tide is found in the MLT. This, however, cannot rule out the possibility that interactions may occur at lower altitudes (e.g. in the stratosphere). Actually, the structured differences between control and base simulations seen below 80 km probably implicate that nonlinear interaction between planetary wave and tide does occur at lower altitudes, although it is weak with the tidal amplitudes being small.

In this simulation, the wavenumber 1 planetary wave is applied at the lower boundary at mid-high latitudes in the northern hemisphere. This is an arbitrary choice and mainly for demonstrative purpose. At this time of the year, the planetary wave could also be generated in the lower southern hemisphere and propagate upward into the MLT region. Depending on the wind condition, it may or may not cross the equator [*Liu et al.*, 2004]. We also note that the variability and nonlinear interaction in the simulation only involve wavenumber 1 components as the primary planetary wave source, because those are the only components specified at the lower boundary in the control simulation. In reality, the interaction could be more complex with the presence of higher wavenumber planetary wave components. The semi-diurnal tide in the control simulation also shows significant variability in this period of time, but it is not discussed here because the semi-diurnal tide is generally much weaker in TIME-GCM.

5. Conclusion

TIMED/SABER and TIDI observations suggest the presence of planetary wave(s) during the time from September 18 to October 1, 2003 when very large tidal variability was found from the near continuous CSU lidar measurement. These results corroborate the various planetary wave periods identified in the lidar observation, and indicate that the large tidal variability may result from interactions between planetary waves and tides. This possibility is examined by using TIME-GCM simulations without and with a transient planetary wave specified at the model lower boundary. Results from TIME-GCM simulation with the transient planetary wave, sampled from the perspective of SABER and TIDI, are qualitatively similar to the SABER and TIDI observations. At the same time, the TIME-GCM simulation with the transient planetary wave also displays strong tidal variability resembling that derived from the lidar observations. The numerical simulations demonstrate that the tidal variability occurs on a global scale as a result of the tidal/PW interaction. The interaction excites non-migrating tides, and the diurnal zonally symmetric component is the strongest. The diurnal eastward wavenumber 1 component is also large as a result of the secondary nonlinear interaction between the zonally symmetry component and the planetary wave. Apart from the excitation of non-migrating tides, the tidal/PW interaction also leads to modulation of the migrating tides. For the diurnal migrating tide, the modulation of the (1, 1) mode is most evident at low latitudes. At mid-high latitudes, the modulation of the trapped modes, especially (1,-2), constitutes a significant portion of the total migrating diurnal tidal variability. The transient planetary wave also excites planetary scale perturbations between 4-10 days, with the most dominating wavenumber 1 component resembling the 5-7-day wave. The wave period is also reflected in the modulation of the migrating diurnal tide at all latitudes. The exact mechanism of this modulation is worth further study. This comparative study thus demonstrates that interactions between transient planetary waves and tides can cause large tidal variability.

Acknowledgments. We thank T. Matsuo for helpful discussions and three anonymous reviewers for their comments. The work at NCAR is supported in part by the NASA Sun Earth Connection Theory Program (S-13753-G). The work done at Colorado State University is supported in part by grants from National Aeronautics and Space Administration, NAG5-10076 and NNX07AB64G, and from National Science Foundation, ATM-0545221. J. Oberheide's work is supported by the DFG through its priority program CAWSES through grant OB 299/2-1. This work was also supported in part by the Chinese Academy of Sciences International Partnership Program for Creative Research Teams. Partial support for JYX to visit NCAR was provided by the NASA Office of Space Science. The National Center for Atmospheric Research is operated by the University Corporation for Atmospheric Research under the sponsorship of the National Science Foundation.

References

Angelats i Coll, M., and J. M. Forbes (2002), Nonlinear interactions in the upper atmosphere: The s=1 and s=3 nonmigrating semidiurnal tides, *J. Geophys. Res.*, *107*, doi:10.1029/2001JD001525.

Azeem, S. M. I., T. L. Killeen, R. M. Johnson, Q. Wu, and D. A. Gell (2000), Space-time analysis of TIMED Doppler interferometer (TIDI) measurements, *Geophys. Res. Lett.*, *20*, 3297–3300.

Chapman, S., and R. S. Lindzen (1970), *Atmospheric Tides*, 200 pp., D. Reidel Publishing Co., Dordrecht, Holland.

Chen, H., M. A. White, D. A. Krueger, and C.-Y. She (1996), Daytime mesopause temperature measurements using a sodium-vapor dispersive Faraday filter in lidar receiver, *Opt. Lett.*, *21*, 1003–1005.

Dickinson, R. E., E. C. Ridley, and R. G. Roble (1981), A three-dimensional general circulation model of the thermosphere, *J. Geophys. Res.*, *86*, 1499–1512.

Dickinson, R. E., E. C. Ridley, and R. G. Roble (1984), Thermospheric general circulation with coupled dynamics and composition, *J. Atmos. Sci.*, *41*, 205–219.

Forbes, J. M. (1995), Tidal and planetary waves, in *The Upper Mesosphere and Lower Thermosphere: A Review of Experiment and Theory*, edited by R. M. Johnson and T. L. Killeen, no. 87 in Geophysical Monograph Series, p. 356, Americal Geophysical Union.

Forbes, J. M., M. E. Hagan, X. Zhang, and J. Hackney (1999), Upper atmosphere tidal variability due to latent heat release in the tropical troposphere, *Adv. Space Res.*, *24*, 1515–1521.

Hagan, M. E., and J. M. Forbes (2002), Migrating and nonmigrating diurnal tides in the middle and upper atmosphere excited by tropospheric latent heat release, *J. Geophys. Res.*, *107*, 4754.

Hagan, M. E., and J. M. Forbes (2003), Migrating and nonmigrating semidiurnal tides in the upper atmosphere excited by tropospheric latent heat release, *J. Geophys. Res.*, *108*, 1062.

Hagan, M. E., and R. G. Roble (2001), Modeling diurnal tidal variability with the national center for atmospheric research thermosphere-ionosphere-mesosphere-electrodynamics general circulation model, *J. Geophys. Res.*, *106*, 24,869–24,882.

Hagan, M. E., C. McLandress, and J. M. Forbes (1997), Diurnal tidal variability in the upper mesosphere and lower thermosphere, *Ann. Geophys.*, *15*, 1176–1186.

Hagan, M. E., M. D. Burrage, J. M. Forbes, J. Hackney, W. J. Randel, and X. Zhang (1999), GSWM-98: Results for migrating solar tides, *J. Geophys. Res.*, *104*, 6813–6828.

Jacobi, C. (1999), Nonlinear interaction of planetary waves and the semidiurnal tide as seen from midlatitude mesopause region winds measured at Collm, Germany, *Meteorol. Z.*, *8*, 28–35.

Kamalabadi, F., J. M. Forbes, N. M. Makarov, and Y. I. Portnyagin (1997), Evidence for nonlinear coupling of planetary waves and tides in the Antarctic mesopause, *J. Geophys. Res.*, *102*, 4437–4446.

Killeen, T. L., Q. Wu, D. A. O. S. C. Solomon, W. R. Skinner, R. J. Niciejewski, and D. A. Gell (2006), Timed Doppler Interferometer : Overview and recent results, *J. Geophys. Res.*, *111*, doi:10.1029/2005JA011484.

Killeen, T. L., et al. (1999), Timed Doppler Interferoemter (TIDI), *Proc. SPIE Int. Soc. Opt. Eng*, *3756*, 289–301.

Li, T., C. Y. She, B. P. Williams, T. Yuan, R. L. Collins, L. M. Kieffaber, and A. W. Peterson (2005), Concurrent OH imager and sodium temperature/wind lidar observation of localized ripples over northern Colorado, *J. Geophys. Res.*, *110*, D13110, doi: 10.1029/2004JD004885.

Lieberman, R. S., J. Oberheide, M. E. Hagan, E. E. Remsberg, and L. L. Gordley (2004), Variability of diurnal tides and planetary waves during November 1978-May 1979, *J. Atmos. Solar Terr. Phys.*, *66*, 517–528.

Lindzen, R. S. (1981), Turbulence and stress owing to gravity wave and tidal breakdown, *J. Geophys. Res.*, *86*, 9707–9714.

Liu, H.-L., and M. E. Hagan (1998), Local heating/cooling of the mesosphere due to gravity wave and tidal coupling, *Geophys. Res. Lett.*, *25*, 2941–2944.

Liu, H.-L., and J. W. Meriwether (2004), Analysis of a temperature inversion event in the lower mesosphere, *J. Geophys. Res.*, *109*, D02S07, doi:10.1029/2002JD003026.

Liu, H.-L., and R. G. Roble (2002), A study of a self-generated stratospheric sudden warming and its mesospheric/lower thermospheric impacts using coupled TIME-GCM/CCM3, *J. Geophys. Res.*, *107*, doi:10.1029/2001JD001533.

Liu, H.-L., M. E. Hagan, and R. G. Roble (2000), Local mean state changes due to gravity wave breaking modulated by diurnal tide, *J. Geophys. Res.*, *105*, 12,381–12,396.

Liu, H.-L., R. G. Roble, M. J. Taylor, and W. R. Pendleton, Jr (2001), Mesospheric planetary waves at northern hemisphere fall equinox, *Geophys. Res. Lett.*, *28*, 1903–1906.

Liu, H.-L., E. R. Talaat, R. G. Roble, R. S. Lieberman, D. M. Riggin, and J.-H. Yee (2004), 6.5-day wave and its seasonal variability in the middle and upper atmosphere, *J. Geophys. Res.*, *109*, D21112, doi:10.1029/2004JD004795.

Mayr, H. G., J. G. Mengel, E. R. Talaat, H. S. Porter, and K. L. Chan (2003), Non-migrating diurnal tides generated with planetary waves in the mesosphere, *Geophys. Res. Lett.*, *30*, 1832.

Mayr, H. G., J. G. Mengel, E. R. Talaat, H. S. Porter, and K. L. Chan (2005a), Mesospheric non-migrating tides generated with planetary waves: I. Characteristics, *J. Atmos. Solar Terr. Phys.*, *67*, 959–980.

Mayr, H. G., J. G. Mengel, E. R. Talaat, H. S. Porter, and K. L. Chan (2005b), Mesospheric non-migrating tides generated with planetary waves: II. Influence of generated with planetary of gravity waves, *J. Atmos. Solar Terr. Phys.*, *67*, 981–991.

Mertens, C. J., M. G. Mlynczak, M. Lopez-Puertas, P. P. Wintersteiner, R. H. Picard, J. R. Winick, L. L. Gordley, and J. M. R. III (2001), Retrieval of mesospheric and lower thermospheric kinetic temperature from measurements of CO_2 15-μm Earth limb emission under non-LTE conditions, *Geophys. Res. Lett.*, *28*, 1391–1394.

Mertens, C. J., et al. (2004), SABER observations of mesospheric temperatures and comparisons with falling sphere measurements taken during the 2002 summer MaCWAVE campaign, *Geophys. Res. Lett.*, *31*, L03105, doi:10.1029/2003GL018605.

Murphy, D. J., M. Tsutsumi, D. M. Riggin, G. O. L. Jones, R. A. Vincent, M. E. Hagan, and S. K. Avery (2003), Observations of a nonmigrating component of the semidiurnal tide over Antarctica, *J. Geophys. Res.*, *108*, 4241, doi:10.1029/2002JD003077.

Nakamura, T., D. C. Fritts, J. R. Isler, T. Tsuda, R. A. Vincent, and I. M. Reid (1997), Short-period fluctuations of the diurnal tide observed with low-latitude MF and meteor radars during CADRE: Evidence for gravity wave/tidal interactions, *J. Geophys. Res.*, *102*, 26,225–26,238.

Nozawa, S., Y. Ogawa, A. Brekke, T. Tsuda, C. M. Hall, H. Miyaoka, J. Kurihara, T. Abe, and R. Fujii (2006), EISCAT observational results during the DELTA campaign, *Earth Planets Space*, *58*, 1183–1191.

Oberheide, J., M. E. Hagan, R. G. Roble, and D. Offermann (2002), Sources of nonmigrating tides in the tropical middle atmosphere, *J. Geophys. Res.*, *107*, 4567.

Oberheide, J., M. E. Hagan, and R. G. Roble (2003), Tidal signatures and aliasing in temperature data from slowly precessing satellites, *J. Geophys. Res.*, *108*, 1055, doi: 10.1029/2002JA009585.

Oberheide, J., H.-L. Liu, O. A. Gusev, and D. Offermann (2006a), Mesospheric surf zone and temperature inversion layers in early november 1994, *J. Atmos. Solar Terr. Phys.*, *68*, 1752–1763.

Oberheide, J., Q. Wu, T. L. Killeen, M. E. Hagan, and R. G. Roble (2006b), Diurnal nonmigrating tides from timed doppler interferometer wind data: Monthly climatologies and seasonal variations, *J. Geophys. Res.*, *111*, A10S03, doi:10.1029/2005JA011491.

Ortland, D. A., and M. J. Alexander (2006), Gravity wave influence on the global structure of the diurnal tide in the mesosphere and lower thermosphere, *J. Geophys. Res.*, *111*, A10S10.

Pancheva, D. V. (2000), Evidence for nonlinear coupling of planetary waves and tides in the lower thermosphere over Bulgaria, *J. Atmos. Solar Terr. Phys.*, *62*, 115–132.

Pancheva, D. V. (2006), Quasi-2-day wave and tidal variability observed over Ascension Island during January/February 2003, *J. Atmos. Solar Terr. Phys.*, *68*, 390–407.

Pancheva, D. V., and N. J. Mitchell (2004), Planetary waves and variability of the semidiurnal tide in the mesosphere and lower thermosphere over Esrange (68°N, 21°E) during winter, *J. Geophys. Res.*, *109*, A08307.

Pancheva, D. V., and P. Mukhtarov (2000), Wavelet analysis on transient behaviour of tidal amplitude fluctuations observed by meteor radar in the lower thermosphere above Bulgaria, *Ann. Geophys.*, *18*, 316–331.

Pancheva, D. V., P. Mukhtarov, N. J. Mitchell, A. G. Beard, and H. G. Muller (2000), A comparative study of winds and tidal variability in the mesosphere/lower-thermosphere region over Bulgaria and the UK, *Ann. Geophys.*, *18*, 1304–1315.

Pancheva, D. V., et al. (2002), Global-scale tidal variability during the PSMOS campaign of June-August 1999: interaction with planetary waves, *J. Atmos. Solar Terr. Phys.*, *64*, 1865–1896.

Richmond, A. D., E. C. Ridley, and R. G. Roble (1992), A thermosphere/ionosphere general circulation model with coupled electrodynamics, *Geophys. Res. Lett.*, *19*, 601–604.

Roble, R. G. (1995), Energetics of the mesosphere and thermosphere, in *The Upper Mesosphere and Lower Thermosphere: A Review of Experiment and Theory*, edited by R. M. Johnson and T. L. Killeen, no. 87 in Geophysical Monograph Series, p. 356, Americal Geophysical Union.

Roble, R. G., and E. C. Ridley (1994), A thermosphere-ionosphere-mesosphere-electrodynamics general circulation model (TIME-GCM): Equinox solar cycle minimum simulations (30-500 km), *Geophys. Res. Lett.*, *21*, 417–420.

Roble, R. G., E. C. Ridley, and R. E. Dickinson (1987), On the global mean structure of the thermosphere, *J. Geophys. Res.*, *92*, 8745–8758.

Roble, R. G., E. C. Ridley, A. D. Richmond, and R. E. Dickinson (1988), A coupled thermosphere/ionosphere general circulation model, *Geophys. Res. Lett.*, *15*, 1325–1328.

Russell, J. M., M. G. Mlynczak, L. L. Gordley, J. J. J. Tansock, and R. W. Esplin (1999), An overview of the saber experiment and preliminary calibration results, *Proc. SPIE Int. Soc. Opt. Eng*, *3756*, 277–288.

Salby, M. L., F. Sassi, P. Callaghan, D.-L. W. P. Keckhut, and A. Hauchecorne (2002), Mesospheric inversions and their relationship to planetary wave structure, *J. Geophys. Res.*, *107*, 4041, doi:10.1029/2001JD000756.

Sassi, F., R. R. Garcia, B. A. Boville, and H.-L. Liu (2002), On temperature inversions and the mesospheric surf zone, *J. Geophys. Res.*, *107*, doi:10.1029/2001JD001525.

She, C.-Y., et al. (2004), Tidal perturbations and variability in mesopause region over Fort Collins, CO (41N, 105W): Continuous multi-day temperature and wind lidar observations, *Geophys. Res. Lett.*, *31*, L24111, doi:10.1029/2004GL021165.

Talaat, E. R., J. H. Yee, and X. Zhu (2001), Observations of the 6.5-day wave in the mesosphere and lower thermosphere, *J. Geophys. Res.*, *106*, 20,715–20,723.

Taylor, M. J., W. R. P. Jr., H.-L. Liu, C. Y. She, L. C. Gardner, R. G. Roble, and V. Vasoli (2001), Large amplitude perturbations in mesospheric oh meinel temperatures around the autumnal equinox transition period, *Geophys. Res. Lett.*, *28*, 1899–1902.

Ward, W. E., V. I. Fomichev, and S. Beagley (2005), Nonmigrating tides in equinox temperature fields from the extended Canadian Middle Atmosphere Model (CMAM), *Geophys. Res. Lett.*, *32*, L03803.

Wu, Q., T. L. Killeen, D. A. Ortland, S. C. Solomon, R. D. Gablehouse, R. M. Johnson, W. R. Skinner, R. J. Niciejewski, and S. J. Franke (2006), TIMED Doppler Interferometer (TIDI) observations of migrating diurnal and semi-diurnal tides, *J. Atmos. Solar Terr. Phys.*, *68*, 408–417.

Xu, J., C.-Y. She, W. Yuan, C. J. Mertens, M. G. Mlynczak, and J. M. Russell, III (2006), Comparison between the temperature measurements by TIMED/SABER and lidar in the midlatitude, *J. Geophys. Res.*, *111*, A10S09, doi:10.1029/2005JA011439.

Zhang, X. L., J. M. Forbes, M. E. Hagan, J. M. Russell, S. E. Palo, C. J. Mertens, and M. G. Mlynczak (2006), Monthly tidal temperatures 20-120 km from TIMED/SABER, *J. Geophys. Res.*, *111*, A10S08, doi:10.1029/2005JA011504.

Figure 1. The amplitudes (a and c) and phases (b and d) of diurnal tidal temperature (a and b) and zonal wind (c and d) at 90 km derived from the CSU lidar measurements between days 264-273 (universal time) of 2003. The blue diamonds are data points and red lines are error bars.

Figure 2. Temperature measured by SABER during ascending (upper panel) and descending (lower panel) orbit nodes for days 266-268 2003 at 40°N.

Figure 3. Meridional (upper panel) and zonal (lower panel) winds measured by TIDI on the cold side during ascending orbit node for days 264, 267 and 268 2003 at 40°N. Unit: ms^{-1}.

Figure 4. SATUT sampling of TIME-GCM temperature from SABER (a) ascending and (b) descending orbit nodes for day 267 and (c) zonal wind and (d) meridional wind in TIDI ascending orbit node on the cold side for day 268 at 40°N.

Figure 5. Total diurnal temperature (a and b) and zonal wind (c and d) amplitudes from base case (a and c) and control case (b and d) TIME-GCM simulations on day 267. The contour intervals for (a) and (b) are 2.5 K. The contour intervals for (c) and (d) are 5 ms^{-1}.

Figure 6. Amplitudes (a and c) and phases (b and d) of total diurnal tidal temperature (a and b) and zonal wind (c and d) from base case (dotted line) and control case (solid line) TIME-GCM simulations at ∼91 km, 42.5°N and 105°W.

Figure 7. Amplitudes of diurnal migrating and nomigrating tidal temperature from base and control TIME-GCM simulations at ∼91 km and 42.5°N. Solid line: Diurnal migrating tide from the control simulation; dotted line: diurnal migrating tide from base case simulation; dash line: diurnal eastward wavenumber 1 tide; dash-dot line: diurnal wavenumber 0 tide; dash-triple-dot: diurnal westward wavenumber 2 tide. All the non-migrating components are from the control simulations.

Figure 8. Differences in the amplitudes of the (a) migrating (b) eastward wavenumber 1 (c) wavenumber 0 and (d) westward wavenumber 2 components of the diurnal tide between the control and base cases. The contour intervals are 1 K in (a), (b), and (d), and 2 K in (c).

Figure 9. The temporal evolution of the (a) quasi-stationary planetary wave wavenumber 1 component at 62.5°N, the diurnal (b) eastward wavenumber 1 component, (c) wavenumber 0 component, and (d) westward wavenumber 2 component of the geopotential height perturbation at 42.5°N from the control case. The temporal evolution of the differences in the amplitudes of the migrating diurnal tidal components of the geopotential height perturbations between the control and base cases at (e) 2.5°N and (f) 52.5°N. Contour intervals: (a) 100 m, (b) 25 m, (c) 25 m, (d) 25 m, (e) 25 m, and (f) 50 m. In (e) and (f) solid lines indicates amplitude increase.

Figure 10. (a)Migrating diurnal tide of the geopotential height perturbations at 0 UT on day 267 from the base case. Projection of the migrating diurnal tide onto (b) (1,1) (c) (1,-1) and (d) (1,-2) Hough modes. Contour intervals: 100 m in (a) and (b); 25 m in (c) and (d).

Figure 11. Decomposition of the total geopotential height migrating diurnal perturbations (black curve) into 4 gravity modes (1,1), (1,2), (1,3) and (1,4) and 4 rotational modes (1,-1), (1,-2), (1,-3) and (1,-4) at 42.5°N and 100 km altitude. Solid curves: control case; dash curves: base case.

Figure 12. Differences in amplitudes of the migrating diurnal tidal geopotential height perturbations for the (1,1) (left), (1,-1) (middle) and (1,-2) (right) modes between the control and base cases for day 264. Contour intervals: 10 m.

Figure 13. Temporal evolution of the differences of the amplitudes of the migrating diurnal tidal geopotential height perturbations for the (1,1) (left), (1,-1) (middle) and (1,-2) (right) modes between the control and base cases at 2.5°N, 52.5°N and 52.5°N, respectively. Contour intervals: 10 m.

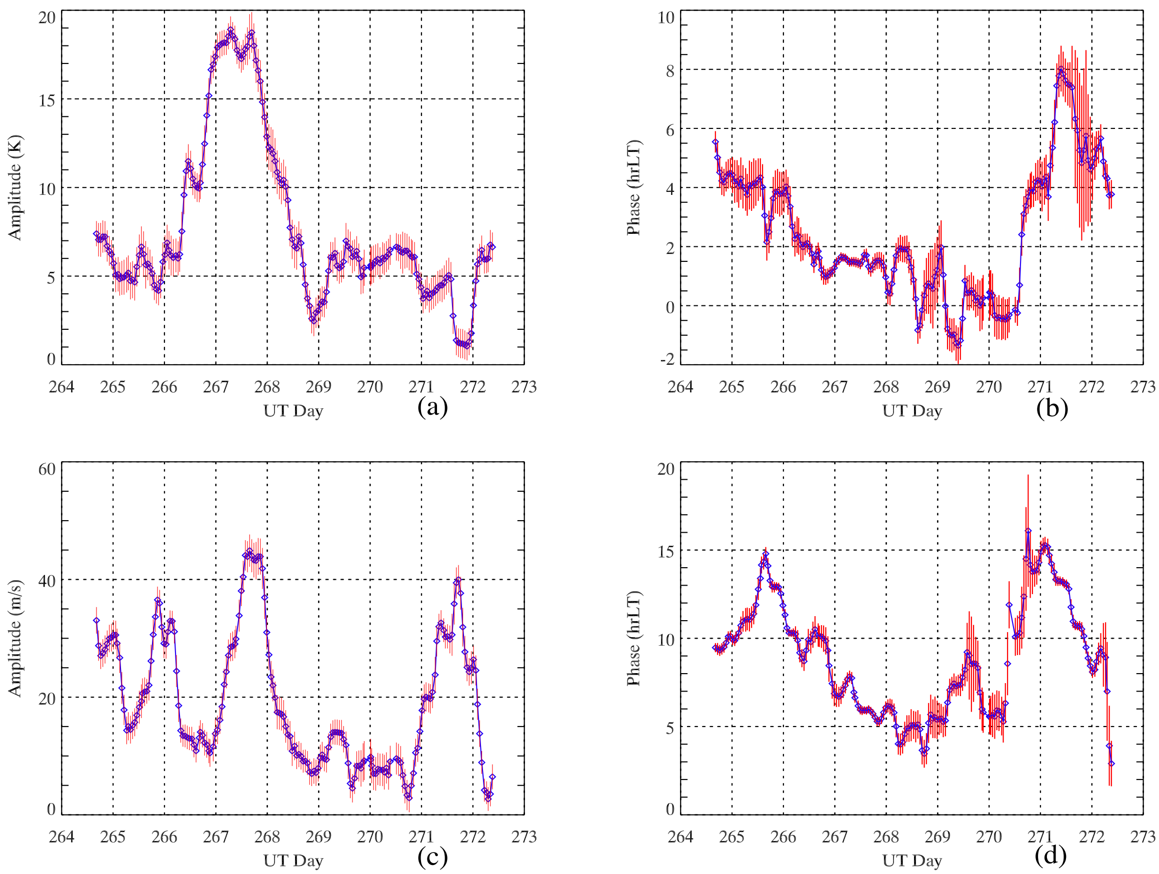

Figure 1.

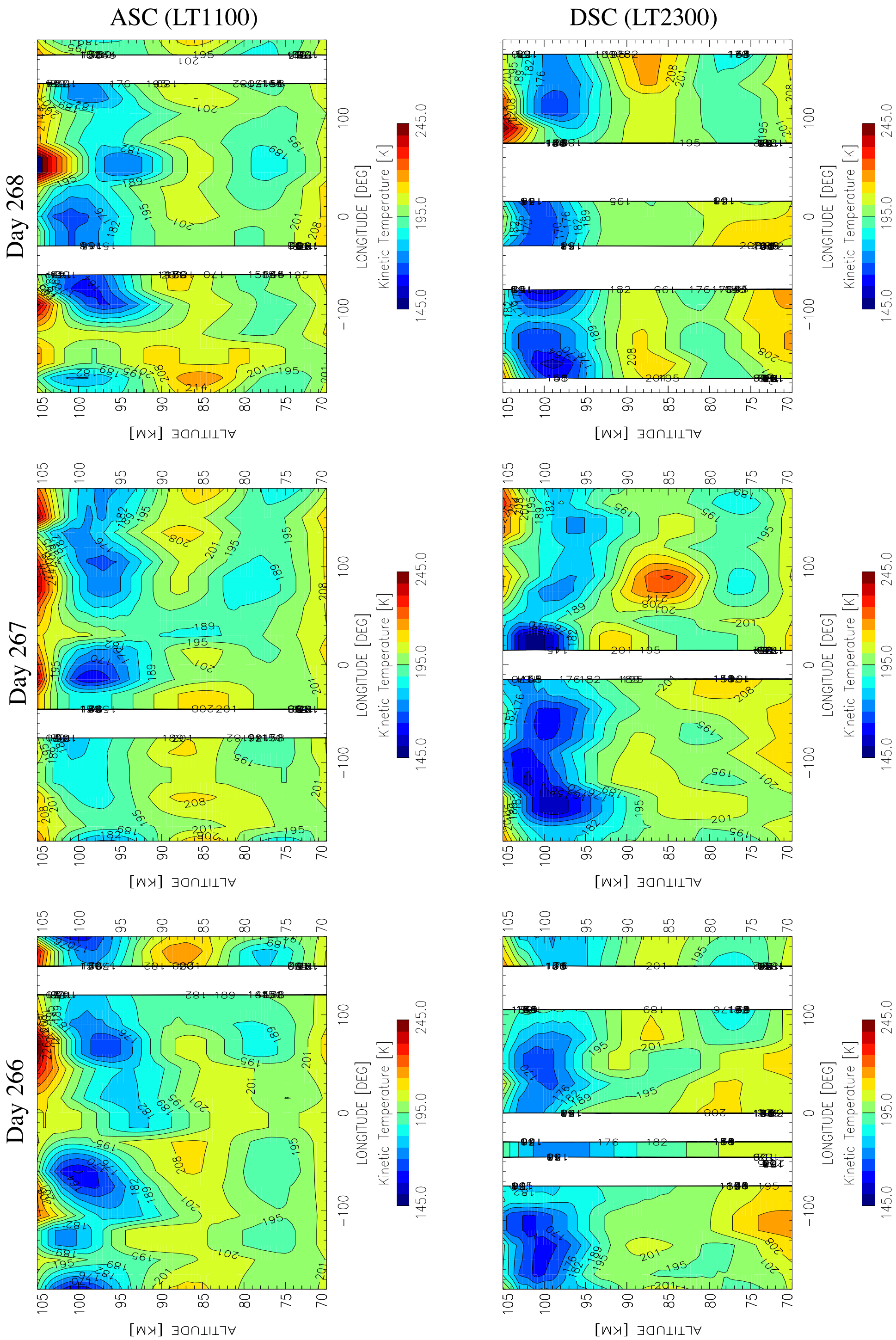
ASC (LT1100)
DSC (LT2300)
Day 268
Day 267
Day 266
ALTITUDE [KM]
LONGITUDE [DEG]
Kinetic Temperature [K]
145.0
195.0
245.0

Figure 2.

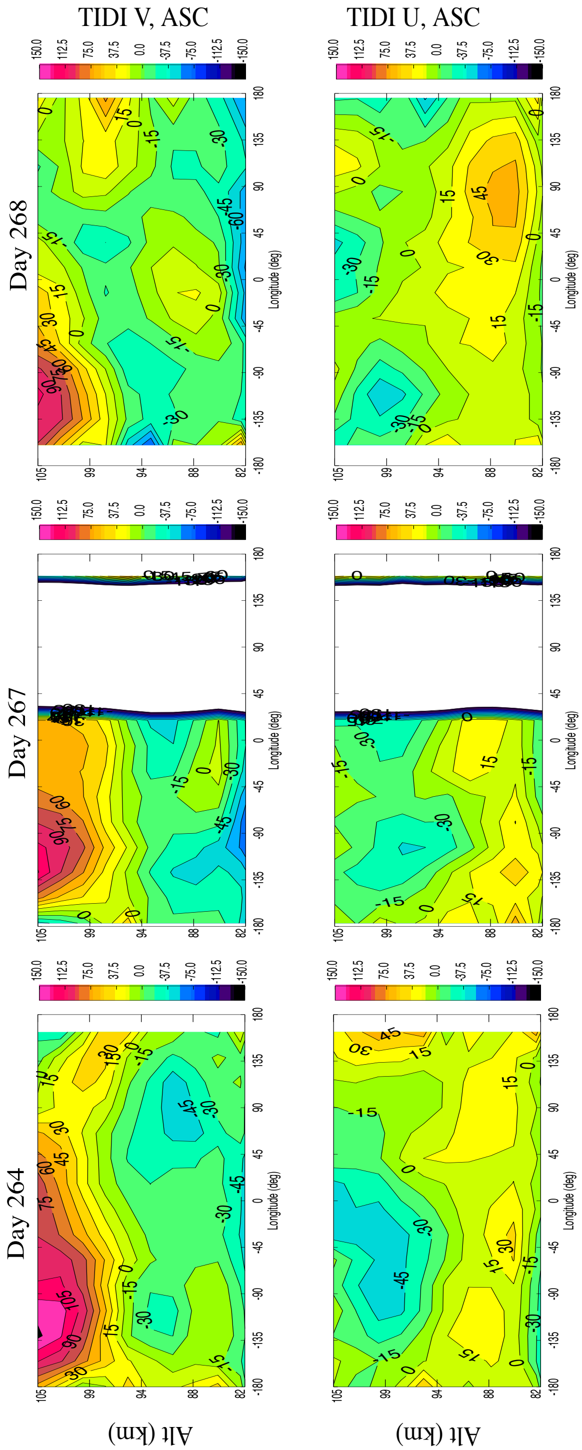
TIDI V, ASC
TIDI U, ASC
Day 264
Day 267
Day 268
Alt (km)
Longitude (deg)

Figure 3.

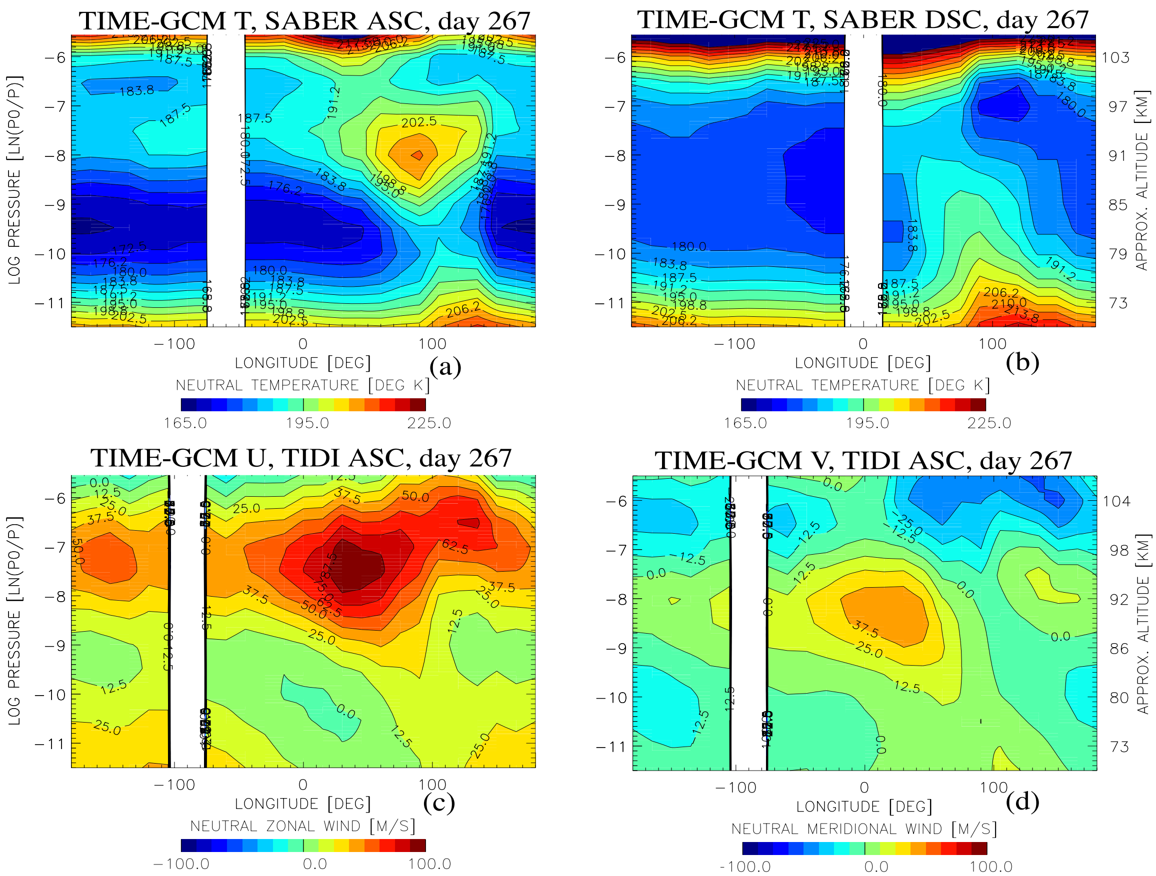
TIME-GCM T, SABER ASC, day 267
LOG PRESSURE [LN(P0/P)]
LONGITUDE [DEG]
(a)
NEUTRAL TEMPERATURE [DEG K]
165.0
195.0
225.0
TIME-GCM T, SABER DSC, day 267
APPROX. ALTITUDE [KM]
LONGITUDE [DEG]
(b)
NEUTRAL TEMPERATURE [DEG K]
165.0
195.0
225.0
TIME-GCM U, TIDI ASC, day 267
LOG PRESSURE [LN(P0/P)]
LONGITUDE [DEG]
(c)
NEUTRAL ZONAL WIND [M/S]
−100.0
0.0
100.0
TIME-GCM V, TIDI ASC, day 267
APPROX. ALTITUDE [KM]
LONGITUDE [DEG]
(d)
NEUTRAL MERIDIONAL WIND [M/S]
-100.0
0.0
100.0

Figure 4.

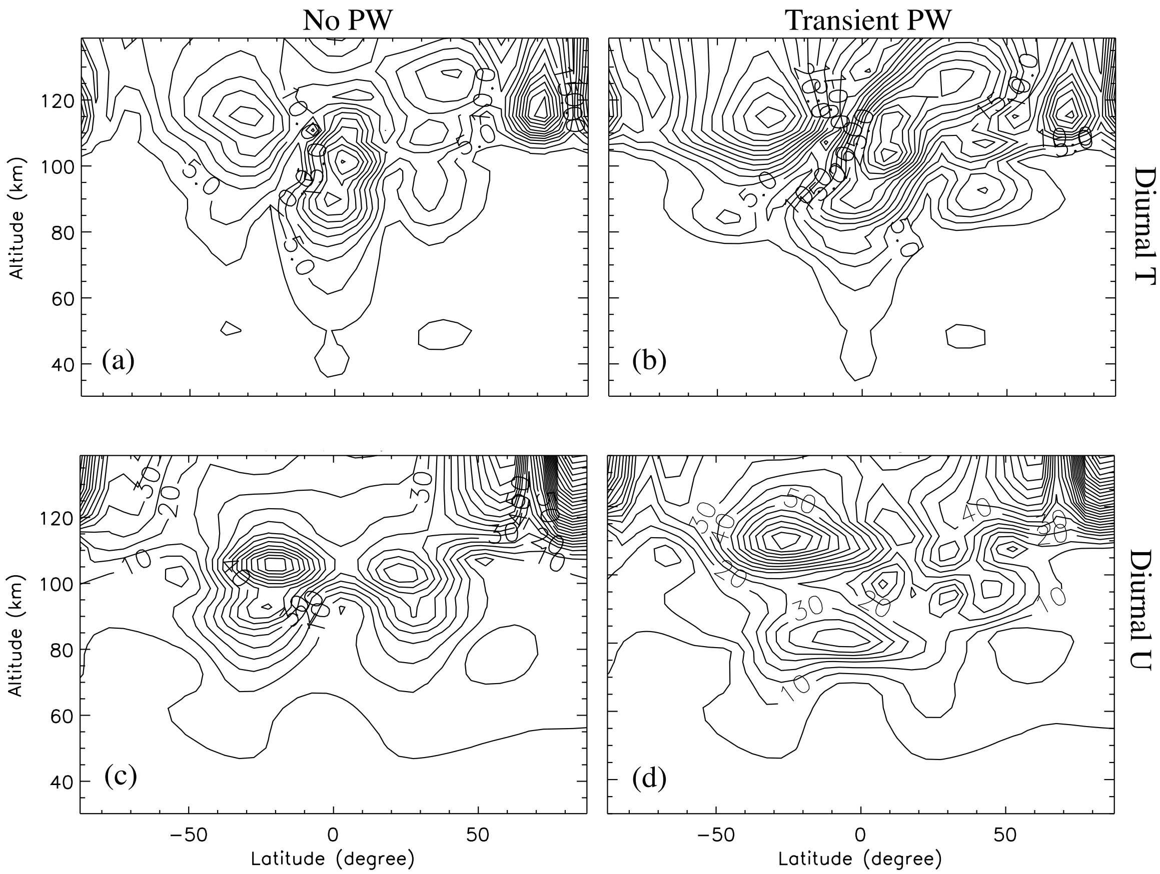
No PW
Transient PW
Diurnal T
Diurnal U
Altitude (km)
Latitude (degree)
(a)
(b)
(c)
(d)

Figure 5.

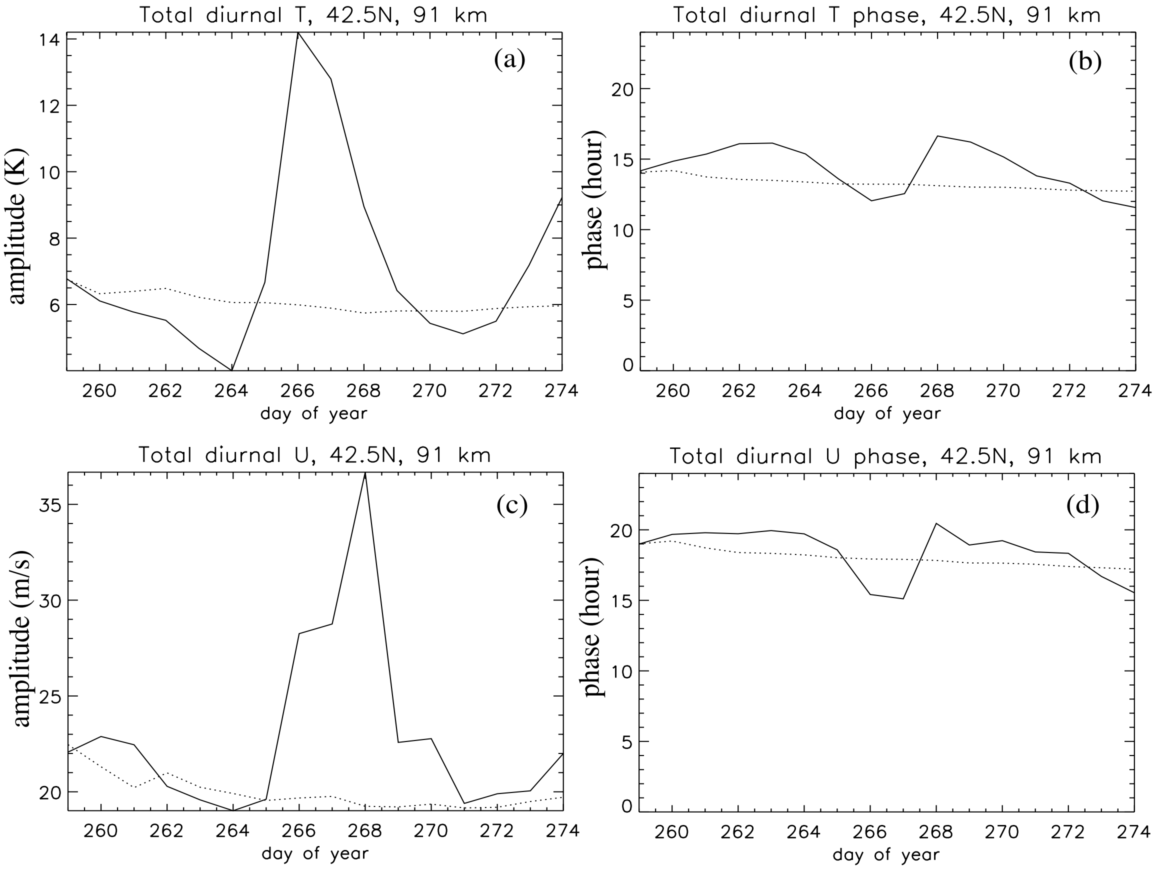
Total diurnal T, 42.5N, 91 km
(a)
amplitude (K)
day of year
Total diurnal T phase, 42.5N, 91 km
(b)
phase (hour)
day of year
Total diurnal U, 42.5N, 91 km
(c)
amplitude (m/s)
day of year
Total diurnal U phase, 42.5N, 91 km
(d)
phase (hour)
day of year

Figure 6.

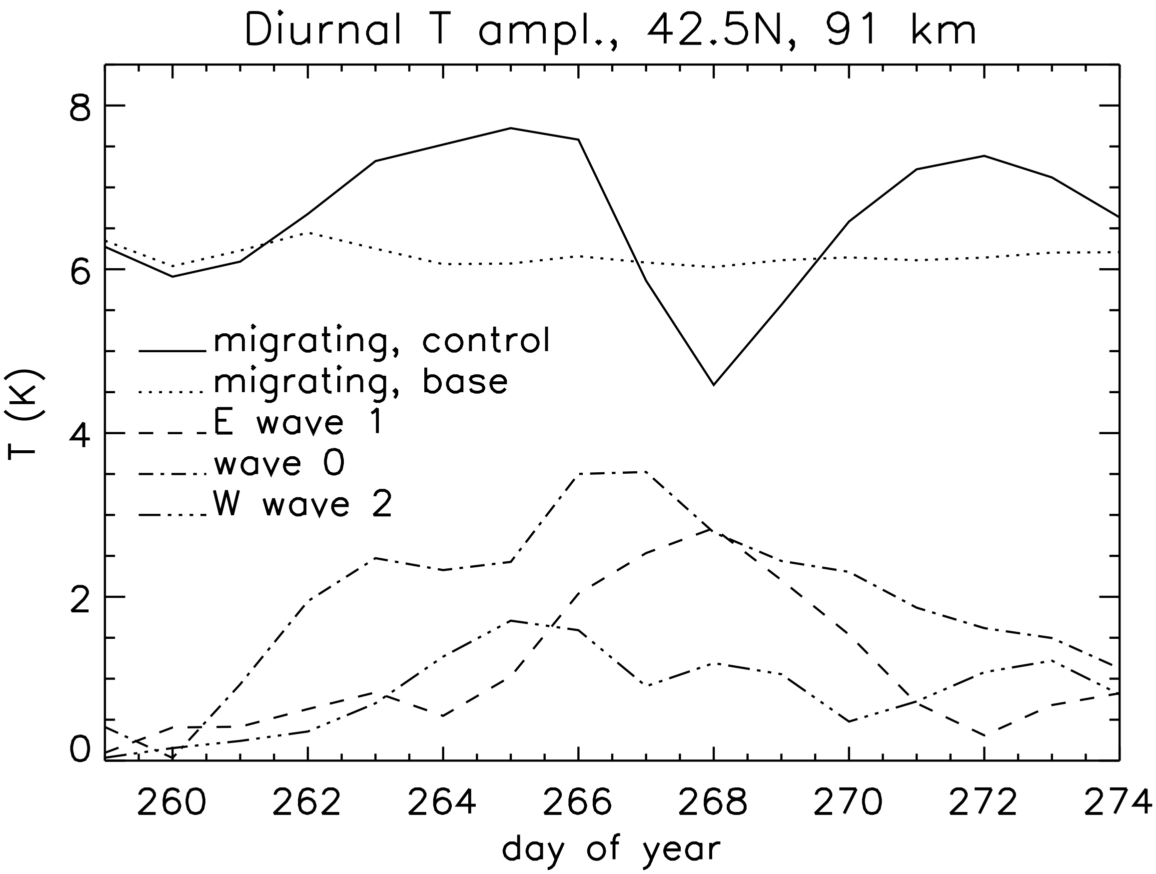
Diurnal T ampl., 42.5N, 91 km
8
6
4
2
0
T (K)
migrating, control
migrating, base
E wave 1
wave 0
W wave 2
260
262
264
266
268
270
272
274
day of year

Figure 7.

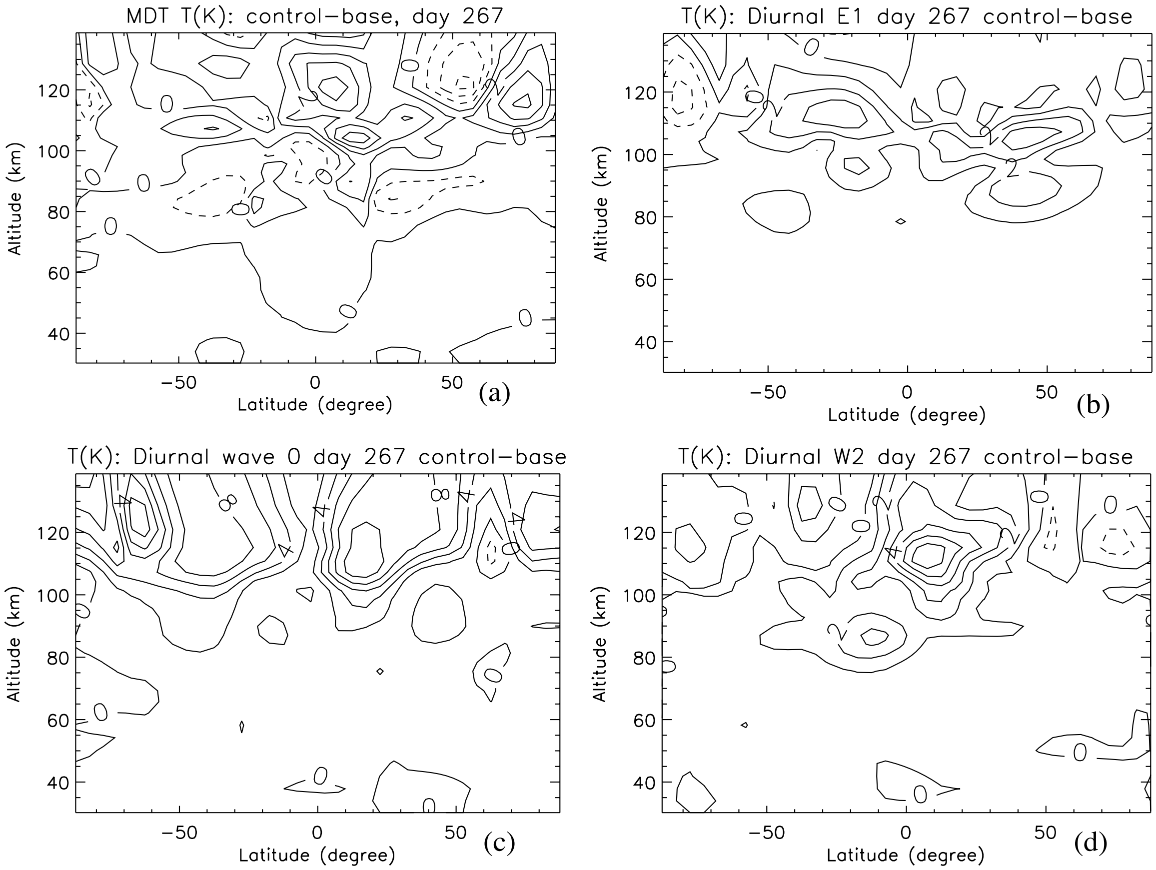

MDT T(K): control−base, day 267
T(K): Diurnal E1 day 267 control−base
T(K): Diurnal wave 0 day 267 control−base
T(K): Diurnal W2 day 267 control−base
Altitude (km)
Latitude (degree)
(a)
(b)
(c)
(d)

Figure 8.

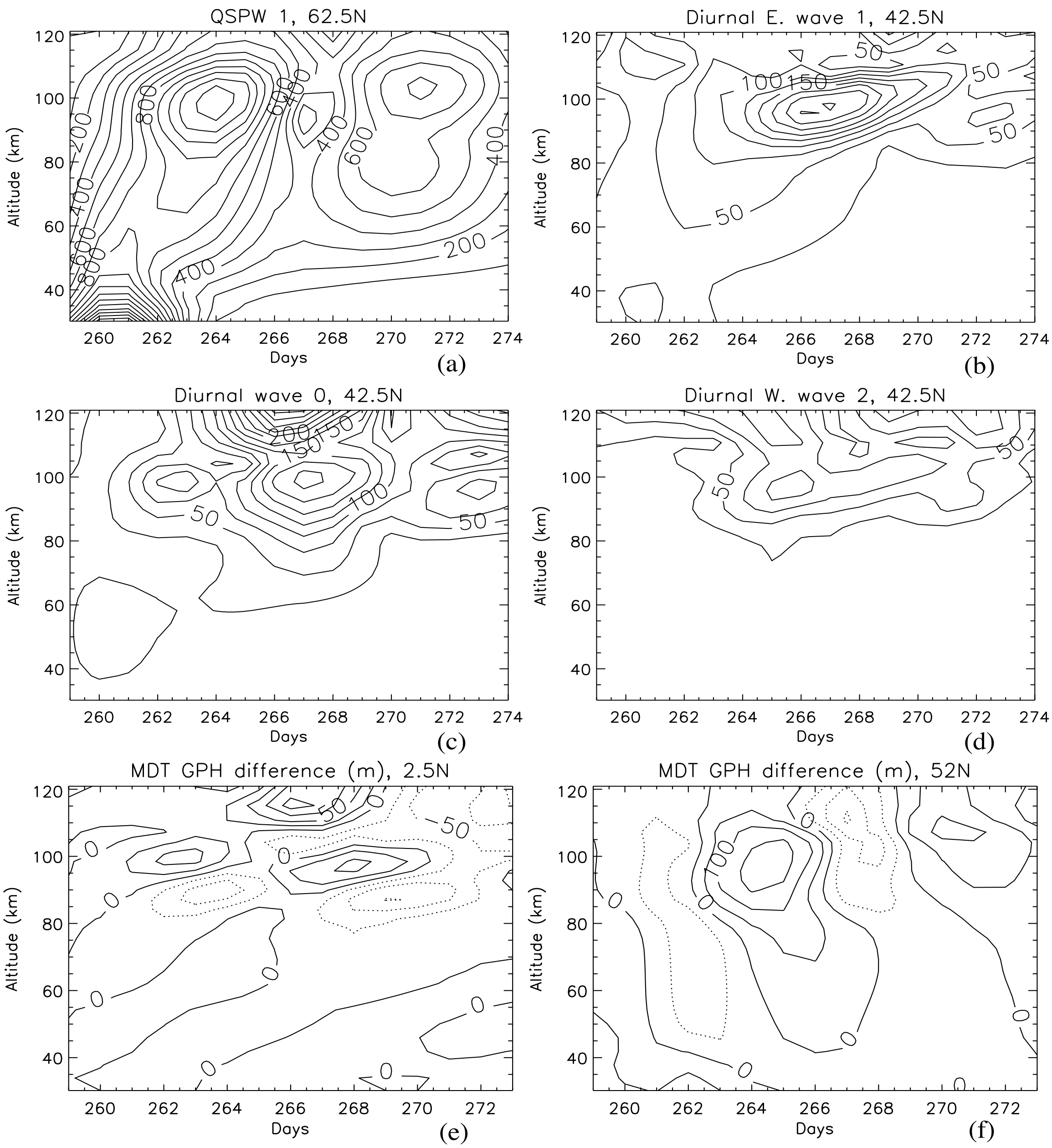
QSPW 1, 62.5N
Diurnal E. wave 1, 42.5N
Diurnal wave 0, 42.5N
Diurnal W. wave 2, 42.5N
MDT GPH difference (m), 2.5N
MDT GPH difference (m), 52N
Altitude (km)
Days
(a)
(b)
(c)
(d)
(e)
(f)

Figure 9.

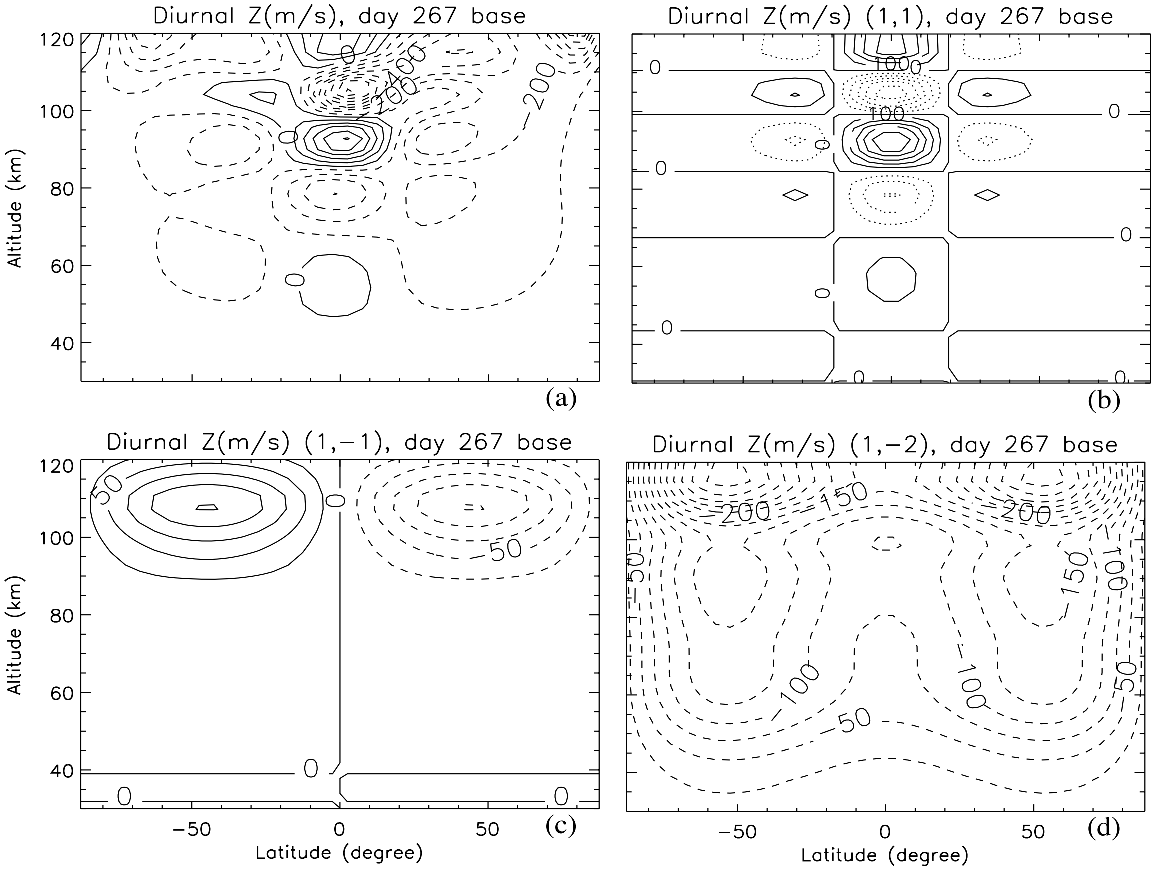
Diurnal Z(m/s), day 267 base
Diurnal Z(m/s) (1,1), day 267 base
Diurnal Z(m/s) (1,−1), day 267 base
Diurnal Z(m/s) (1,−2), day 267 base
Altitude (km)
Latitude (degree)
(a)
(b)
(c)
(d)

Figure 10.

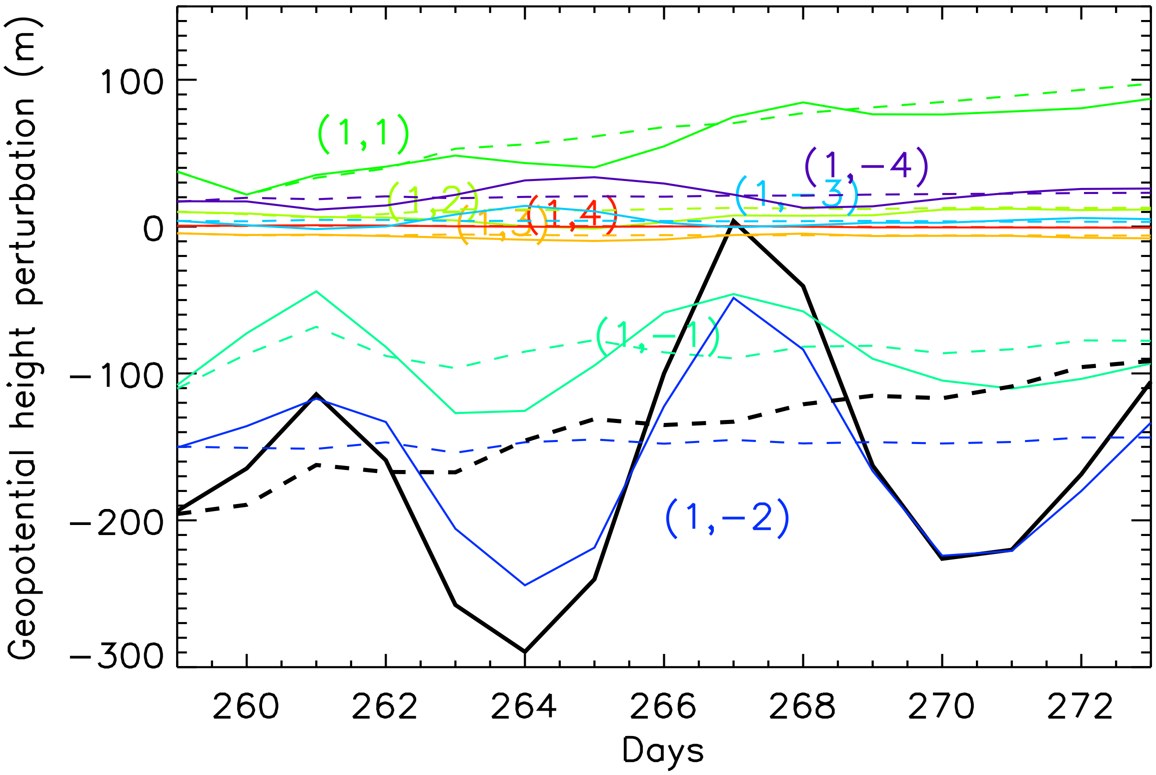

Geopotential height perturbation (m)
100
0
−100
−200
−300
260
262
264
266
268
270
272
Days
(1,1)
(1,2)
(1,3)
(1,4)
(1,−4)
(1,−3)
(1,−1)
(1,−2)

Figure 11.

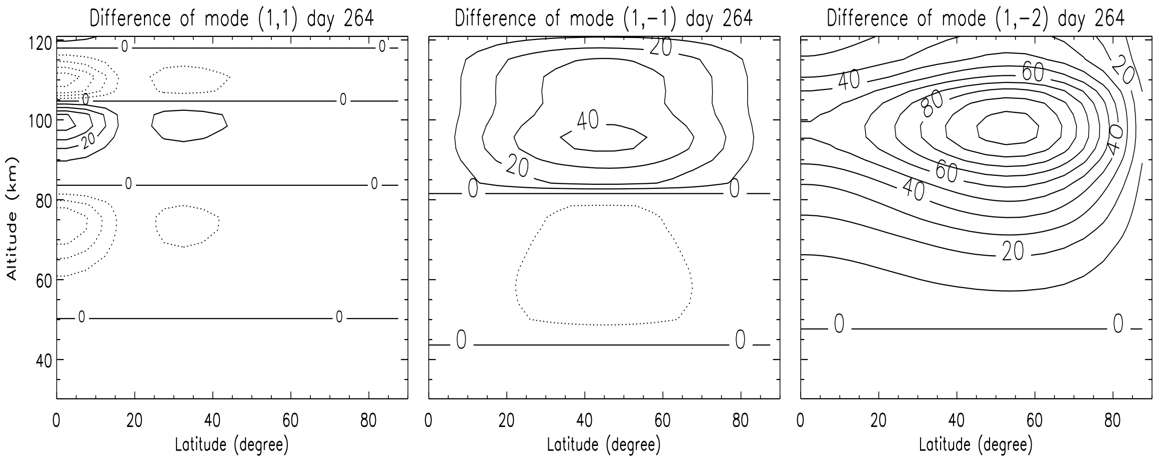
Difference of mode (1,1) day 264
Difference of mode (1,−1) day 264
Difference of mode (1,−2) day 264
Altitude (km)
Latitude (degree)
Latitude (degree)
Latitude (degree)

Figure 12.

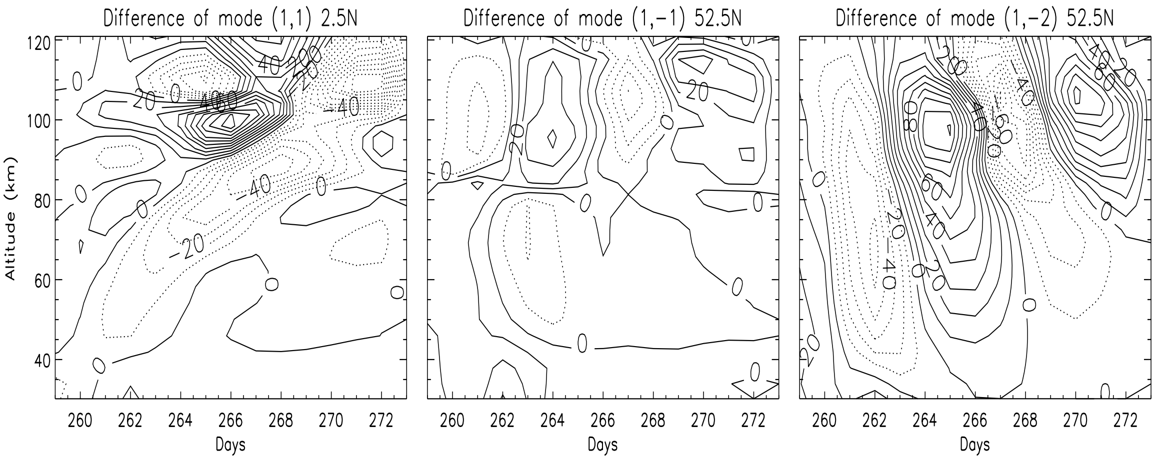
Difference of mode (1,1) 2.5N
Difference of mode (1,−1) 52.5N
Difference of mode (1,−2) 52.5N
Altitude (km)
Days
Days
Days

Figure 13.